

# Chapter 9

## Processing of Lotus Metals

**Abstract** In order to use lotus metals for various industrial products, processing is indispensable. Here, two important topics are chosen: joining technique and severe deformation without shape change of metals.

**Keywords** Equal-channel angular extrusion process • Laser beam • Vickers hardness • Welding

### 9.1 Weldability

#### 9.1.1 Weld Fusion Property of Lotus Copper

For industrial use of the porous metals as various parts, reliable joining techniques such as welding is required as well as processing techniques. There have been some reports on laser and arc welding of foamed aluminum manufactured by using foaming agent,  $\text{TiH}_2$ , or  $\text{CaCO}_3$  [1–3]. However, weldability of porous metals with controlled pore direction such as lotus metals has not been investigated, although the welding is necessary for fabricating engineering materials. Murakami et al. [4] investigated the weldability of lotus copper, and in their study the laser beam with narrow weld bead width and heat-affected zone was applied to the welding of lotus metal. Figure 9.1 shows schematic views of specimens using laser welding. The laser beam was delivered using a 600- $\mu\text{m}$ -diameter optical fiber. The focal length for Nd:yttrium–aluminum–garnet (Nd:YAG) laser with a 1,064-nm wavelength was 100 mm. The diameter of the laser beam at the focus point was 300  $\mu\text{m}$ . The laser beam was irradiated at an  $80^\circ$  forward angle relative to a workpiece surface damage to the optics by a reflection of laser beam. Argon was used as a shielding gas with a flow rate of  $5.0 \times 10^4 \text{ m}^3 \text{ s}^{-1}$ . Figure 9.2 shows a relation between the welding speed and the penetration depth of the weld bead in depth at the thickness of 5 mm from the work piece surface when the laser beam power of 3.2 kW was irradiated on both types of samples (a) and (b) shown in Fig. 9.1. The penetration depth in both directions

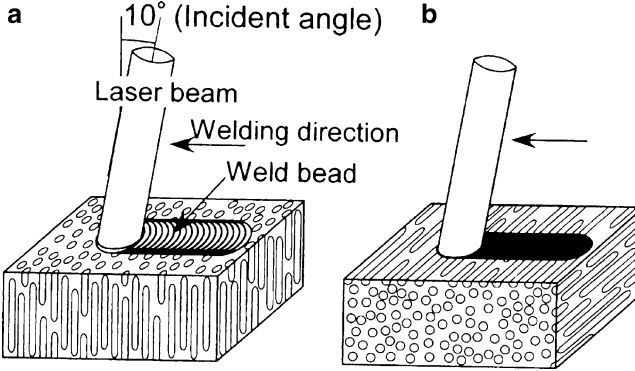


**Fig. 9.1** Schematic views of specimens during laser welding in the lotus copper with the pore growth (a) perpendicular and (b) parallel to the work piece surface (Reprinted with permission from [4] © 2003 Elsevier Science B.V.)

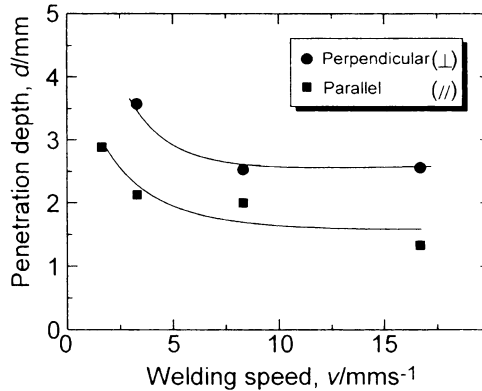


**Fig. 9.2** Relation between welding speed and penetration depth of the weld bead in depth at the thickness of 5 mm from the work piece surface when the laser beam power of 3.2 kW was irradiated on both types of sample (a) and (b) shown in Fig. 9.1 (Reprinted with permission from [4] © 2003 Elsevier Science B.V.)

decreases with increasing welding speed. The penetration depth in the parallel direction (filled square) is always shallower than that in the perpendicular direction (filled circle). Figure 9.3 shows the top view of the specimens after laser welding in the thickness of 5 mm at the constant laser beam power of 3.2 kW in the welding speed range of 1.67–16.7 mm s<sup>-1</sup> in (a)–(c) perpendicular and (d)–(g) parallel pore directions. In the perpendicular direction, only the groove was observed in the condition of 16.7 mm s<sup>-1</sup> as shown in Fig. 9.3a. The weld beads were found below the welding speed of 8.33 mm s<sup>-1</sup> as shown in Fig. 9.3b, c, while a smooth weld bead was observed at the welding speed of 3.33 mm s<sup>-1</sup>. In contrast, in the parallel direction, no weld bead was made in the welding speed range from 3.33 to 16.7 mm s<sup>-1</sup>, and a smooth weld bead on all specimens was not observed. At the

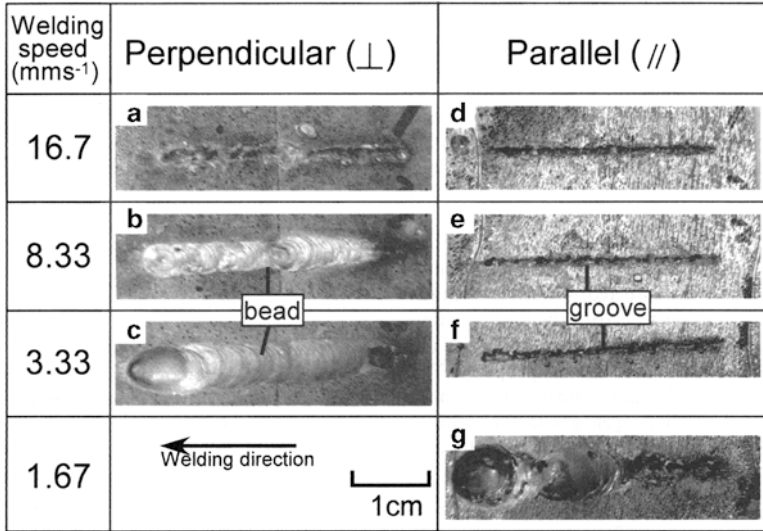


**Fig. 9.3** Top views of laser welded specimen at different welding speeds with 3.2-kW constant laser power in 5-mm thickness in (a–c) perpendicular and (d–g) parallel to the pore growth directions. Welding speed: (a) and (b) 16.7 mm s<sup>-1</sup>, (b) and (e) 8.33 mm s<sup>-1</sup>, (c) and (f) 3.33 mm s<sup>-1</sup>, and (g) 1.67 mm s<sup>-1</sup> (Reprinted with permission from [4] © 2003 Elsevier Science B.V.)

welding speed of 1.67 mm s<sup>-1</sup>, the weld bead was formed only at the end of weld, though nonuniform. These indicate that the formation of the weld bead has strong anisotropy of pore direction in relation to the irradiation direction of laser beam.

The effect of the laser power on the penetration depth in the thickness of 4 mm for two pore directions at the constant welding speed of 3.33 mm s<sup>-1</sup> was shown in Fig. 9.4. The penetration depth of the weld bead perpendicular to the pore growth direction shows a sharp rise at the laser beam power of 2.4 kW. On the other hand, the penetration depth in the parallel to the pore growth direction increases gradually in comparison with that in the perpendicular. These facts indicate that the keyhole formed at the laser-irradiated point perpendicular to the pore growth direction may be attributed to the metal vaporization [5] more than the laser beam power of 2.4 kW, but not in the case parallel to the pore direction. Figure 9.5 shows the cross sections of laser welding direction in the thickness of 4 mm in the welding speed of 3.33 mm s<sup>-1</sup> at the laser beam power of 3.2, 2.5, and 2.0 kW (a)–(c) perpendicular and (d)–(f) parallel to the pore growth directions. As shown in Fig. 9.5a, the weld part at the laser beam power of 3.2 kW in the perpendicular case was completely melted through the bottom; shortly, the fully penetrated weld bead was formed. The shape of the fusion boundary is nearly straight. The straight line of the fusion boundary is nearly parallel to the direction of the original pores. Some large and many small pores in the weld metal were observed in the weld bead. The weld metal at the laser beam power of 2.5 kW in the perpendicular shown in Fig. 9.5b did not

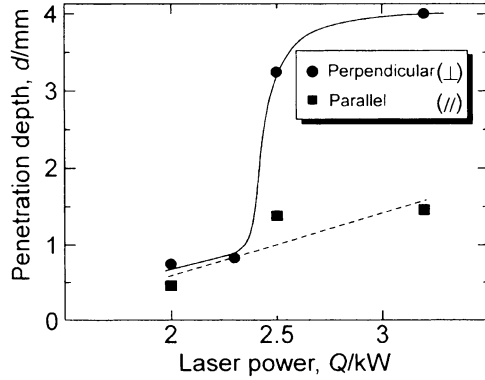


**Fig. 9.4** Effect of laser power on penetration depth of weld bead for perpendicular and parallel to the pore growth direction in depth of 4 mm thick from the work piece surface at  $3.33 \text{ mm s}^{-1}$  welding speed (Reprinted with permission from [4] © 2003 Elsevier Science B.V.)

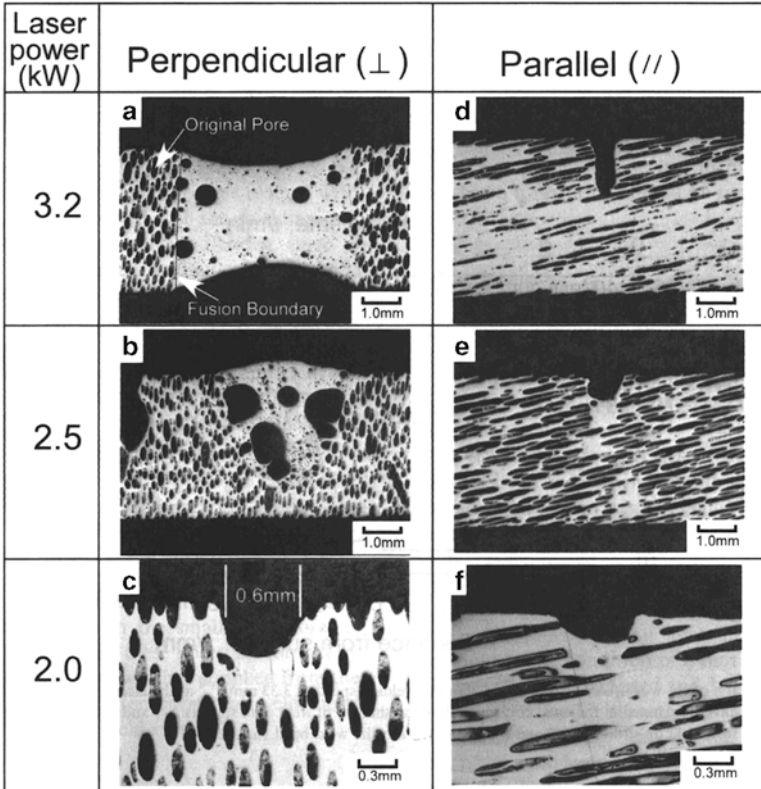


**Fig. 9.5** Cross sections of laser weld perpendicular to the welding direction in 4-mm thickness in the welding speed of  $3.33 \text{ mm s}^{-1}$  at the laser beam power of 3.2, 2.5, and 2.0 kW (a–c) perpendicular and (d–f) parallel to the pore growth directions, which are slightly inclined to the work piece surface with about  $10^\circ$  (Reprinted with permission from [4] © 2003 Elsevier Science B.V.)

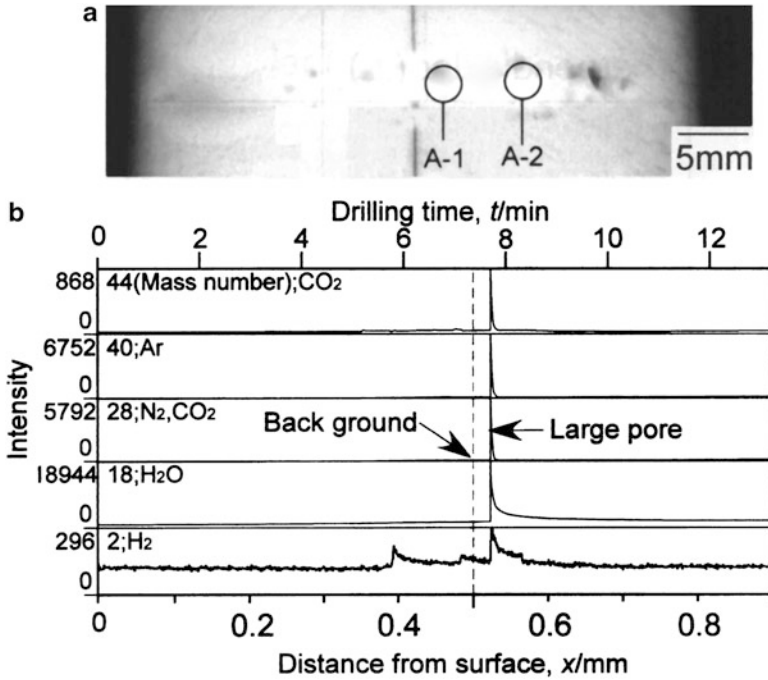


**Fig. 9.6** (a) X-ray radiograph of the workpiece after welding with the welding speed of  $3.33 \text{ mm s}^{-1}$  at the laser beam power of 3.2-kW depth of 4 mm thick. The drilling points determined were in the *open circle* including the shadow of weld pore as A-1 and A-2. (b) Dependence of mass spectral intensity of gas detected from A-2 on drilling time and the distance from the weld bead surface (Reprinted with permission from [4] ©2003 Elsevier Science B.V.)

melt through the opposite side. Some larger pores evolved by the weld were observed in the weld metal. At the laser power of 2.0 kW shown in Fig. 9.5c, the weld metal was not observed, and the diameters of the grooves formed instead of weld bead were about 0.6 mm. In the parallel direction case, the shape of groove was similar to Fig. 9.5c, though the groove depth increased with increasing laser power. Obviously, the shape of the weld bead and the groove exhibits anisotropy with respect to the pore growth direction. Thus, the weldability of lotus copper in the perpendicular direction is more significant than that in the parallel direction.

X-ray radiograph of the work piece after welding with the welding speed of  $3.33 \text{ mm s}^{-1}$  at the laser beam power of 3.2 kW taken in depth of 4 mm thick is shown in Fig. 9.6a. The weld bead after welding was drilled in 3-mm diameter in the vacuum chamber, and the residual gas in the pores was analyzed using a mass spectrometer. The drilling points were determined in the open circle including the shadow of the weld pores such as A-1 and A-2. Figure 9.6b shows the drilling time and the distance from the weld bead surface dependence of mass spectral intensity of residual gas detected from the pores in weld metal (Fig. 9.5a) with the welding speed of  $3.33 \text{ mm s}^{-1}$  at the laser beam power of 3.2 kW in depth of 4 mm thick.

When the drilling depth increases to more than 0.5 mm, various kinds of gases were clearly detected at the same time with high intensity, which were evolved from the large weld pore at this point. These gases are identified as  $H_2$ ,  $H_2O$ ,  $N_2$ , Ar, and  $CO_2$  by the mass spectrometer. No obvious change in the intensity was detected during drilling for other gases up to 100 mass numbers. The gas concentration was determined using a net intensity, which eliminated the difference between the peak intensity and the background intensity in depth of 0.5 mm from the surface. Some small hydrogen peaks with comparably high intensity were detected in depth of 0.4 and 0.48 mm. These may correspond to small weld pores which were formed during welding. The major component of A-1 was argon comprised beyond 73 vol.%, and other components were 14 vol.% nitrogen and water. The major component of A-2 was water which comprised about 60–70 vol.%, and other components were about 20 vol.% argon, several to 10 vol.% nitrogen, and several volume percent hydrogen.

It is generally considered that the pores in the laser weld bead of dense materials are formed by the shielding gas trapped in the weld pool due to keyhole instability by vaporized molten metal [6]. Therefore, it is likely that argon of the shielding gas was detected as a main component. The detected nitrogen may result in the gas from the air which is trapped together with the shielding gas. In their study, however, the presence of a large amount of water and small amount of hydrogen is not explainable in terms of only keyhole instability. The reason why those components are present in the pores is that high-pressure hydrogen gas remains in the closed original pores in the lotus copper formed during the unidirectional solidification under high pressure. It is considered that at remelting of workpiece by laser welding, the remaining hydrogen gas in the original pore was released into the molten weld metal and then coalesced into the large pore which is generated by keyhole instability. Subsequently the hydrogen gas reacted with oxygen containing in air trapped with the shielding gas, and then water vapor was evolved. Besides, there is a small amount of hydrogen gas that does not react with oxygen in some pores. Nitrogen gas in air was also trapped but remained in the pores because of no reaction with molten copper. Similar reason was supposed in the case of  $CO_2$  gas formation. Therefore, the large pores in the weld metal are comprised of the shielding gas, the vaporized copper, the air trapped with the shielding gas, and the hydrogen gas. On the other hand, the small gas pores are composed of the supersaturated hydrogen supplied from the original closed pores in lotus copper.

As mentioned above, significant anisotropy in the morphology of laser weld metal was observed, depending on the pore growth direction. The laser beam mostly reflects on the copper surface due to the high reflectivity of copper [7, 8]. A part of the laser beam penetrates deeply into the pores in the lotus copper with cylindrical pores perpendicular to the welding direction, since the direction of pore growth is nearly identical to the incident laser beam direction; the multiple reflections of the laser beam at the pore inner wall increases the amount of heat input absorbed to the specimen. In addition, two-dimensional thermal conductivity on the parallel plane to the specimen surface is low, which enhances the melting of the specimen. The amount of heat input for the lotus copper with cylindrical pores

parallel to the welding direction is smaller than that of the perpendicular, because of no multiple reflection and high-thermal conductivity. Moreover, the molten copper in the weld pool is blown out more significantly by high-pressure hydrogen gas released from the original closed pores.

In the laser beam welding of lotus copper plate, the pore growth direction should be perpendicular to the work piece surface. When the lotus copper plate with the original pores parallel to the work piece is used, the surface treatment should be required in order to increase the laser beam absorption.

### ***9.1.2 Weld Fusion Property and Joint of Lotus Magnesium***

Figure 9.7 shows the bead appearance and macrostructures in the cross section of the welded specimen with pores perpendicular to the specimen surface at nominal laser power of 0.8, 1.0, and 1.2 kW and spot diameters of 0.3, 0.45, and 0.6 mm [9]. The fusion area of the specimen at the laser power of 0.8 kW and the spot diameter of 0.6 mm did not penetrate to the bottom although complete penetration of the fusion area was achieved for the spot diameter of 0.45 mm as well as for increased laser powers. This is because energy density in the former case is lower than that in the latter case. In the weld metal, some blowholes, which form due to the remnant hydrogen gas in the original closed pores, were observed at the laser power of 1.2 kW and the spot diameter of 0.45 mm, as shown in Fig. 9.7.

Macrostructures of the welded joint with pores parallel to the specimen surface at different nominal laser powers are shown in Fig. 9.8. The weld at the laser powers of 1.5 and 2.0 kW completely melted the bottom, while the weld at the laser power of 1.0 kW did not melt the bottom completely. The blowholes, which are indicated by black arrows in Fig. 9.8, were observed for all the conditions. There were more blowholes in the weld metal of the specimen with pores parallel to the specimen surface (parallel case) than in the weld metal of the specimen with pores perpendicular to the specimen surface (perpendicular case). This was because the blowholes were caused by the remnant hydrogen gas in the original closed pores, and the number of original closed pores for the specimen in the parallel case was much more numerous than that for the specimen in the perpendicular case.

By comparing Fig. 9.7, which represents the laser power of 1.0 kW and the spot diameter of 0.6 mm, with Fig. 9.8a, it was observed that the profiles of the weld metal in the perpendicular and parallel cases were different, although the welding condition was identical. The depth of penetration in the former case is greater than that in the latter case. In the previous report [4], the melting property of lotus copper differed greatly according to the pregrowth direction. The weld bead in the parallel case was not formed in most welding conditions, and only a groove was observed. The difference in the melting property was attributed to the high reflectivity of copper for a laser beam. On the other hand, the reflectivity of magnesium is much lower than that of copper. Therefore, it is expected that the melting property of lotus magnesium is mainly controlled by the thermal conductivity.

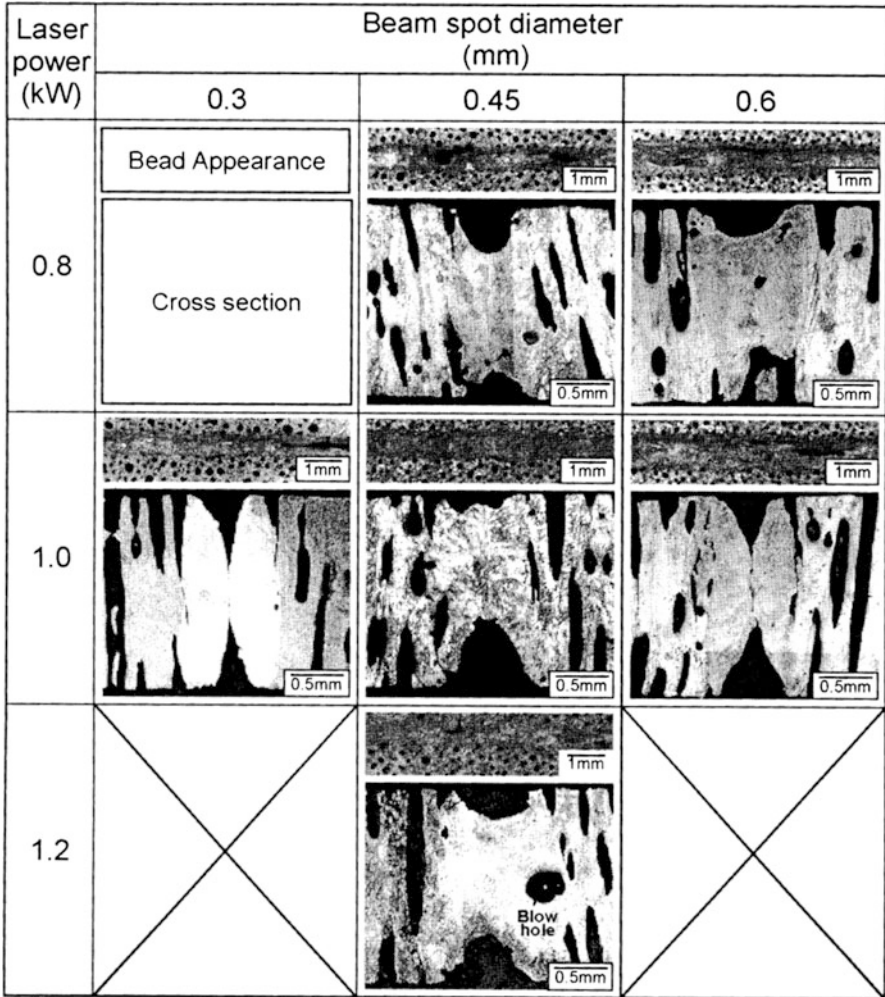
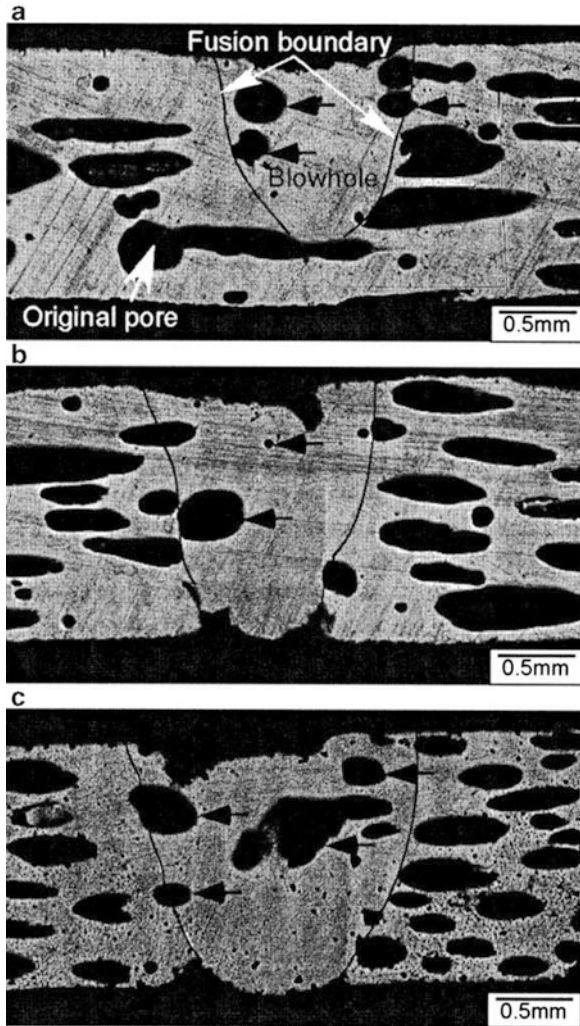


**Fig. 9.7** Bead appearance and macrostructure of laser welded specimen with the pores perpendicular to the specimen surface at the laser powers of 0.8, 1.0, and 1.2 kW and the spot diameters of 0.3, 0.45, and 0.6 mm (Reprinted with permission from [9] ©2006 Elsevier B.V.)

The effect of pore growth direction on the joint strength of lotus magnesium was investigated. Figure 9.9 shows the geometry of tensile specimens of the base metal and the welded joint. A tensile test specimen with a gage section of 1.8 mm × 5 mm was cut out of the specimen before the welding for the base metal and after the welding for the welded joint using the spark erosion wire-cutting machine. The tensile test was performed on the specimen in a tensile test machine at a rate of  $1.67 \times 10^{-2} \text{ mm s}^{-1}$  at room temperature. The tensile strengths of the weld beads and the base metals in the parallel and perpendicular cases are shown in Fig. 9.10



**Fig. 9.8** Macrostructure of welded specimen with the pores parallel to the specimen surface at the spot diameter of 0.6 mm and the laser powers of (a) 1.0 kW, (b) 1.5 kW, and (c) 2.0 kW (Reprinted with permission from [9] © 2006 Elsevier B.V.)



together with the cross-sectional view of the fractured joints. The open and closed circles in Fig. 9.10 denote the samples fractured in the base metal or in the weld bead, respectively. The average tensile strengths of the base metal in the parallel and perpendicular cases were approximately 55 and 30 MPa, respectively. The average tensile strength of the weld bead with the pores perpendicular to the specimen surface was 29 MPa, which was similar to that of the base metal because the joint was fractured in the base metal as shown in Fig. 9.10b. On the other hand, the weld bead in the parallel case was fractured at the joint interface between the weld metal and the base metal as shown in Fig. 9.10a. The average joint strength in the parallel case was 41 MP, which is lower than that of the base metal for the same case.

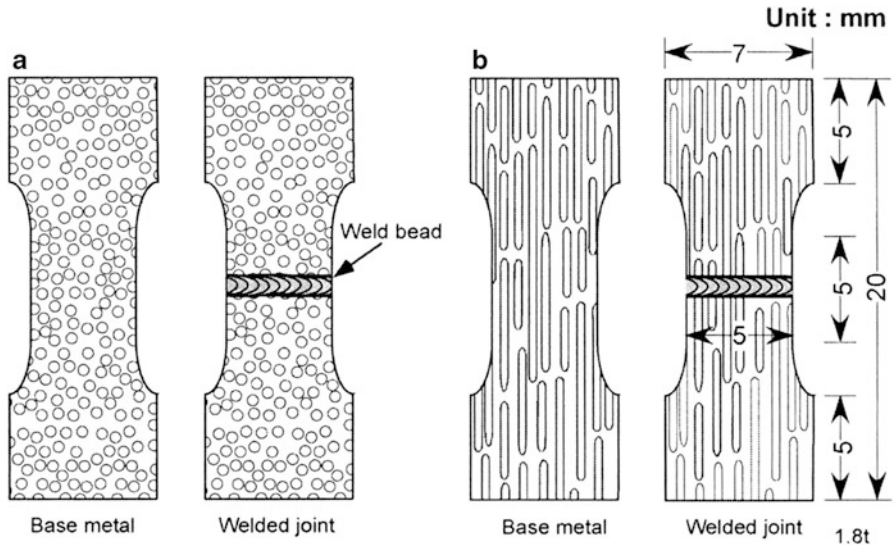


**Fig. 9.9** Geometry in the tensile test specimens of base metal and welded joint with the pores (a) perpendicular and (b) parallel to the specimen surface (Reprinted with permission from [9] © 2006 Elsevier B.V.)

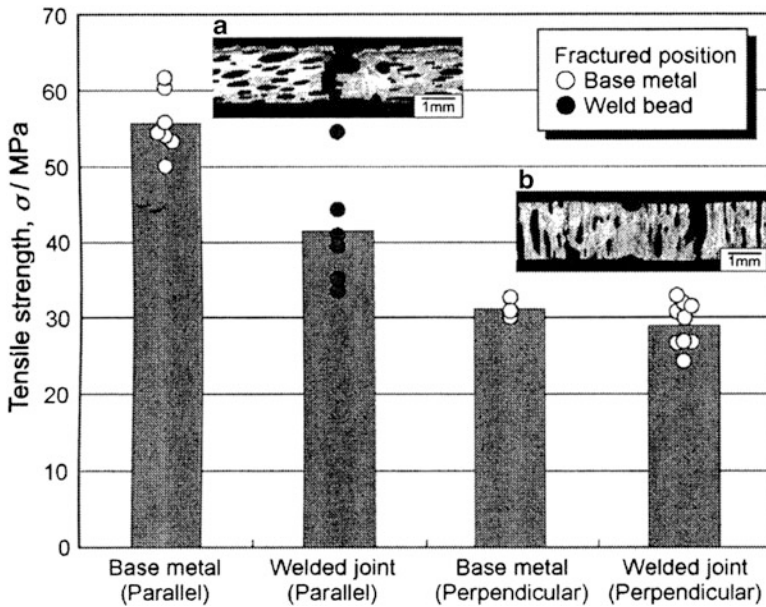


**Fig. 9.10** Tensile strength of the base metal and welded joint with the pores perpendicular and parallel to the specimen surface together with cross section of fractured joint. (a) Fractured in the weld bead and (b) fractured in the base metal (Reprinted with permission from [9] © 2006 Elsevier B.V.)

Ikeda et al. [10, 11] reported the tensile strength of nonporous magnesium produced by unidirectional solidification. The tensile strength parallel to the solidification direction was larger than that perpendicular to the solidification direction. The highly preferred orientations of the nonporous and lotus magnesium fabricated by unidirectional solidification were  $\langle 0002 \rangle$  and  $\langle 11\bar{2}0 \rangle$  [10, 11]. The slip system of magnesium at room temperature is only  $(0002) \langle 11\bar{2}0 \rangle$  [12]. When a load perpendicular to the pore growth direction is applied to porous magnesium with a  $\langle 11\bar{2}0 \rangle$  orientation, the  $(0002) \langle 11\bar{2}0 \rangle$  slip occurs because the normal direction of the  $(0002)$  basal plane is perpendicular to the solidification direction. On the other hand, when a load parallel to the growth direction is applied to porous magnesium with  $\langle 0002 \rangle$  and  $\langle 11\bar{2}0 \rangle$  orientations, the Schmid factor is close to 0. Therefore, the anisotropic tensile strength of the lotus magnesium is controlled not only by the pore growth direction but also by the crystallographic direction.

## 9.2 Equal-Channel Angular Extrusion Process

Suzuki et al. investigated the possibility to improve the mechanical properties of the metallic part of porous metals by plastic deformation [13]. As a kind of porous metals, lotus metals were selected, which are expected to be suitable for improvement of metallic parts by plastic deformation. Since the lotus metals have more metallic parts than metallic foams with up to 90 % of porosity, it is expected that the pores do not disappear and the effect of plastic deformation is obvious. Even if the pores are compressed, metallic part work hardens so that specific strength may increase. The densified materials are expected still to have micro- or nano-pores, which induce novel functions of materials. As a plastic deformation process the equal-channel angular extrusion (ECAE) [14] was adopted as shown in Fig. 9.11. In this process a sample rod is inserted in the entry channel and extruded to the exit channel through a die with a channel angle  $\Phi$ . At the corner between the two channels, the sample is sheared with severe plastic deformation. Because of several advantages, nowadays this process has been investigated actively [15]. First, as the shape and the diameter of the sample rod after the extrusion are the same as that before the extrusion, it is thus possible to extrude the same sample many times through the same die. Secondly, as various processing routes can be selected arbitrarily, it is possible to vary the deformation pattern. Thirdly, lower hydrostatic stress than forging or extrusion does not cause significant densification.

Until now there is no report about ECAE of porous metals. Severe plastic deformation of porous materials has several special characteristics compared with that of nonporous materials because of the densification process and thus requires newly established plastic deformation models. Here the fundamental plastic deformation behavior of lotus copper during ECAE process is described.

**Fig. 9.11** Schematic illustration of ECAE process (Reprinted with permission from [13] © 2008 Elsevier B.V.)

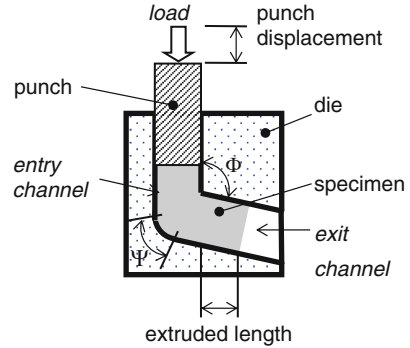


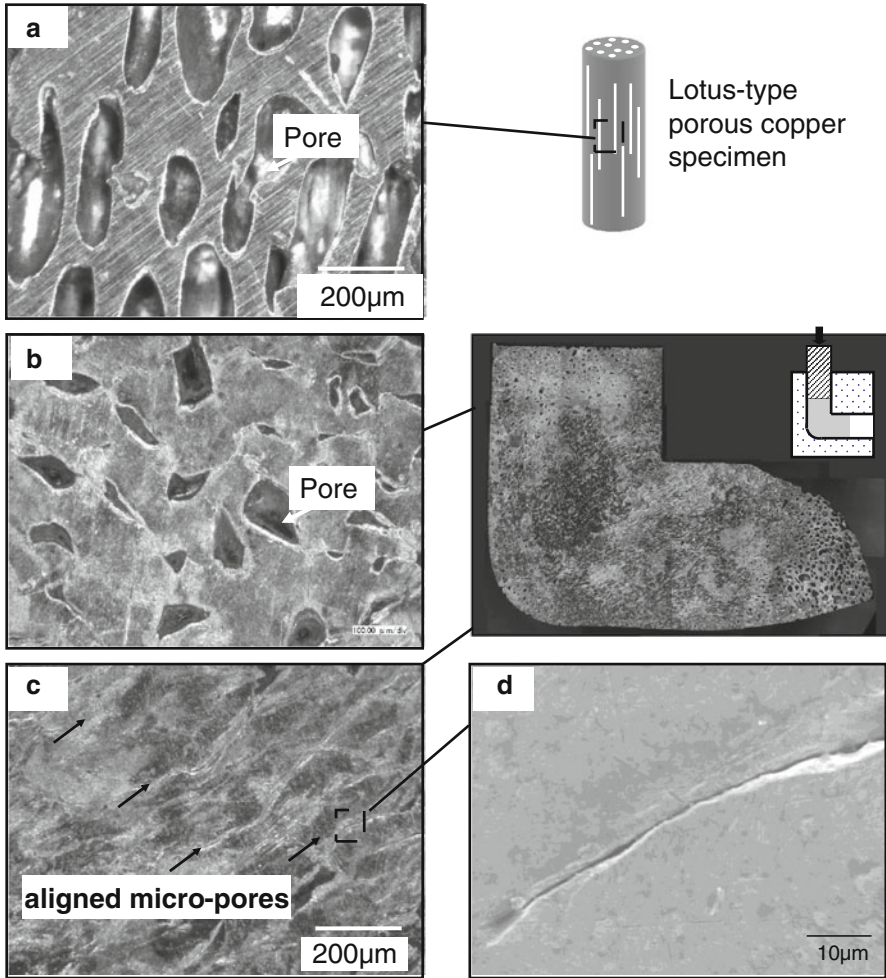
Figure 9.12 shows the cross section of lotus copper which was extruded halfway of the first pass through the die with a channel angle of  $90^\circ$ . In the entry channel part (Fig. 9.12b), some of polygonal shapes still remain, although a lot of pores are seen to be compressed. The pore morphologies are similar to those of specimens deformed uniaxially by compression tests [16]. In the exit channel close to the corner, almost no pores in the original size are observed but many streaks inclined toward the exit channel axis (Fig. 9.12c, d). Many pores remain in the leading end of the specimen, which is the initial unsteady part. Figure 9.13 shows the cross section of the completely extruded sample.

The volume change  $\Delta V$  during the process can be calculated by

$$\Delta V(\%) = \frac{V_0 - V_1}{V_0} \times 100 = \frac{p_0 - p_1}{100 - p_1} \times 100, \quad (9.1)$$

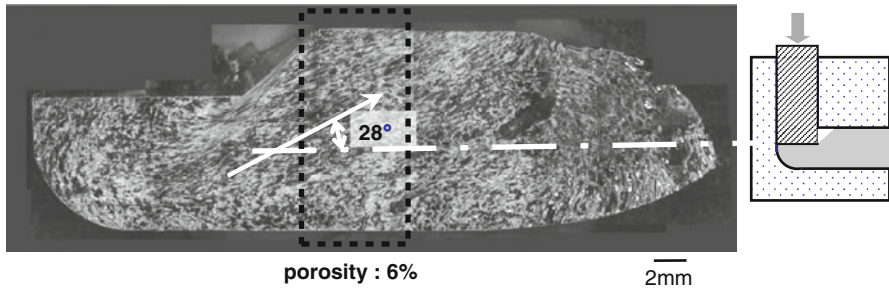
where  $V$  and  $p$  are the volume and the porosity, respectively. The suffixes 0 and 1 mean the states before and after the deformation, respectively. The porosity of the sample cut from the part in the entry channel (Fig. 9.12b) was 17 %, and that in the exit channel, shown within the dotted line in Fig. 9.13 was 6 %. The volume change in the entry channel was calculated to be 40 % with  $p_0 = 50$  % and  $p_1 = 17$  %, and that in the exit channel was calculated to be 12 % with  $p_0 = 17$  % and  $p_1 = 6$  %. As shown in Fig. 9.13, the pores after the shear deformation are inclined from the central axis. This inclination can be explained by using a geometrical model shown in Fig. 9.14. One assumes a square region “klmn” on a cross section of a sample rod (Fig. 9.14a); the square turns and deforms into a parallelogram (Fig. 9.14b) shape by the shear stress at the corner. In the case of nonporous materials, the line “lm” inclines theoretically  $26.5^\circ$  to the exit channel axis [14].

In the case of lotus metals which are densified during the shear deformation, the area “lmn” should be decreased. As the volume reduction by shearing at the corner was 12 %, the area  $S_0$  of the square “klmn” should be reduced. Therefore, the side “nm” reduces from 1 to 0.88 as shown in Fig. 9.14b, and the inclination  $\theta$  of “lm” can be estimated as  $28^\circ$ . The observed inclination of pores agrees well with the estimation. From these results, the deformation behavior during the extrusion through ECAE process can be schematically illustrated in Fig. 9.15.

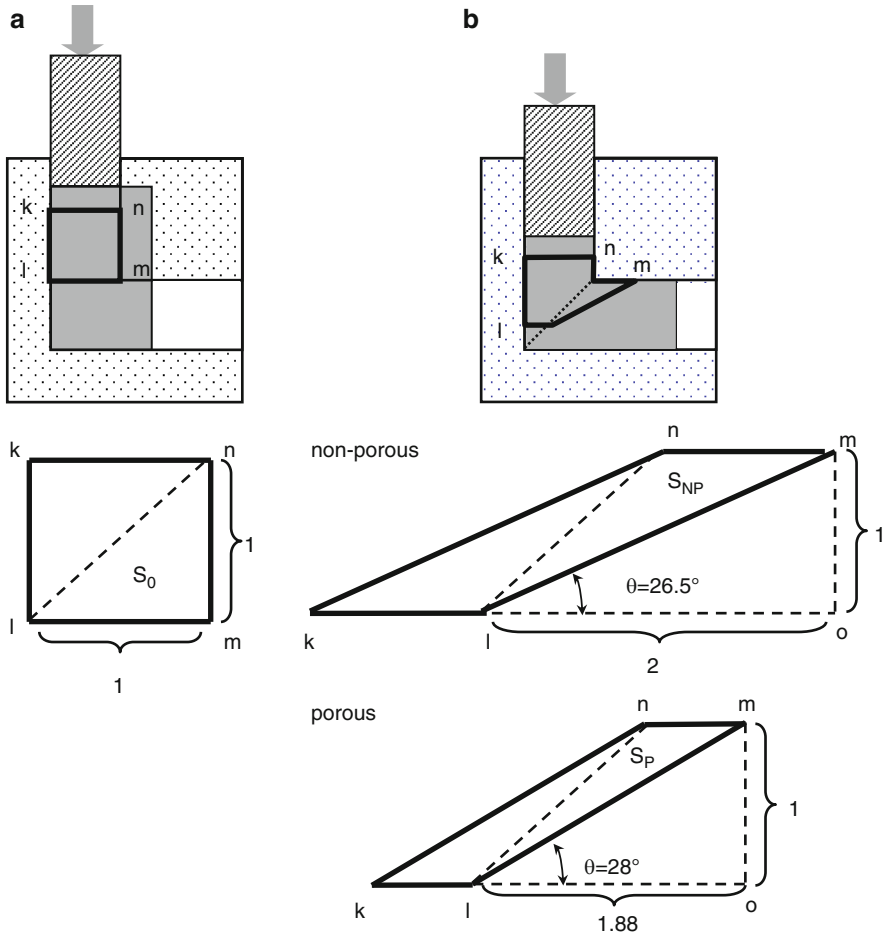


**Fig. 9.12** Cross sections of a lotus copper specimen before and after extrusion approximately 36 mm in a single pass through an ECAE die with a channel angle of 90°. (a) Before extrusion. (b) Compressed part in the entry channel. (c) Shear-deformed part in the exit channel close to the corner. The *arrows* indicate micropores. (d) Micropore magnified in the window in (c) (Reprinted with permission from [13] © 2008 Elsevier B.V.)

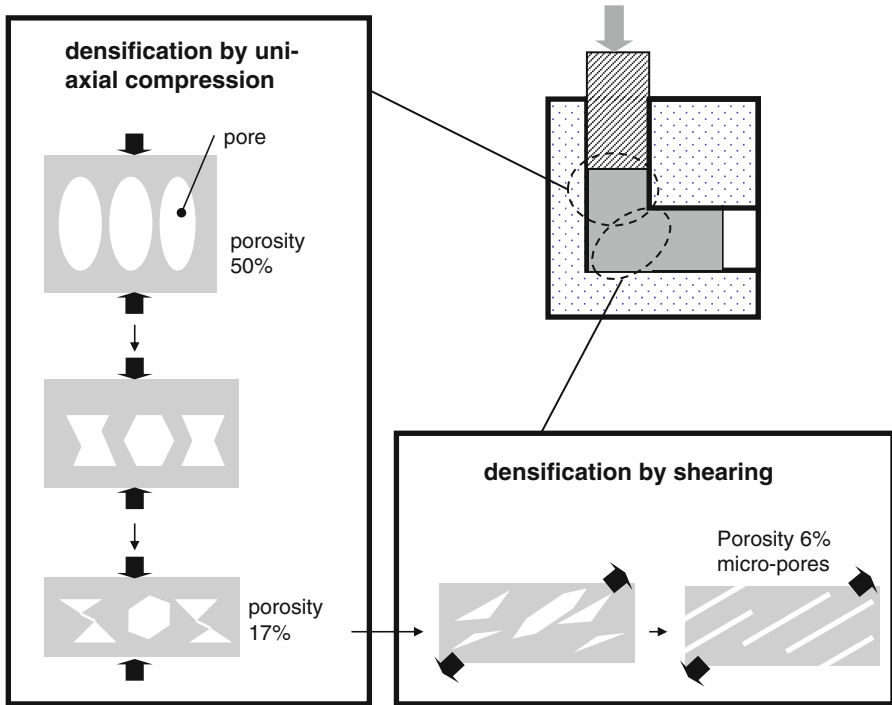
The extruded samples after the second pass are shown in Fig. 9.16a, b. On the cross section of the extruded sample via route A, these pores aligned in one direction are observed. Even after the second pass, the walls of the pores seem not to be bonded, since hydrogen captured in the pores prevented complete compression pores. On the other hand, the pores were opened again in the case of route C where the sample was rotated axially 180° from the first pass. This deformation behavior can also be explained by using the deformation model in Fig. 9.15. It may be possible to change the pore morphology by ECAE process.



**Fig. 9.13** Cross section of a lotus copper specimen after completely extruded through an ECAE die with a channel angle of  $90^\circ$  in a single pass. The porous metal within the *square* drawn with a *dotted line* has a porosity of 6 % (Reprinted with permission from [13] © 2008 Elsevier B.V.)



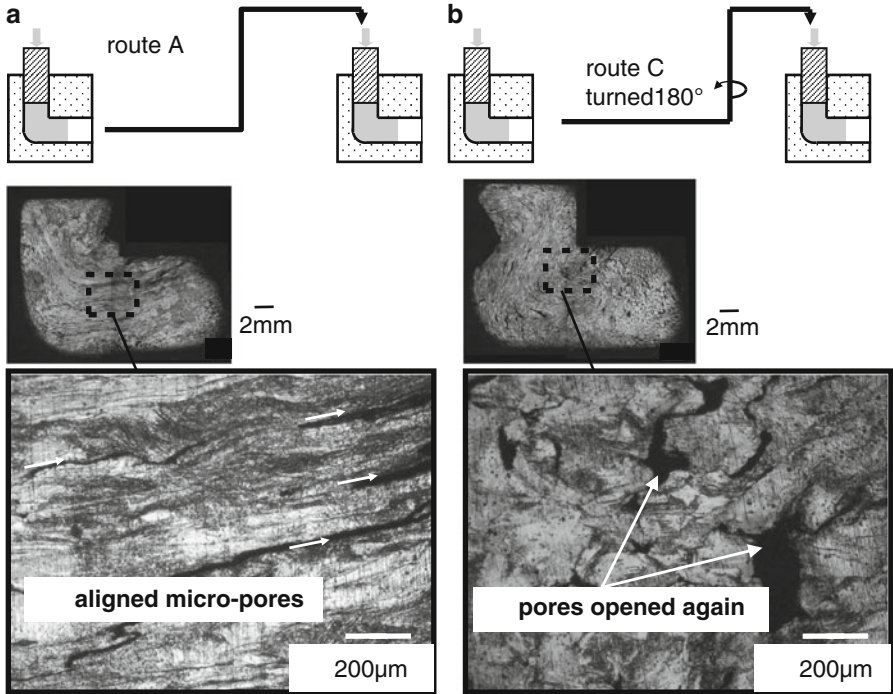
**Fig. 9.14** Geometrical model for the deformation behavior of sample rod through ECAE process with a channel angle of  $90^\circ$ . A square “klmn” on the cross section shown in (a) turns and deforms into a parallelogram shown in (b). The area  $S_0$  of the square “klmn” in the entry channel is the same as the area SNP of “klmn” in the exit channel.  $S_p$  is 12 % smaller than  $S_0$  (Reprinted with permission from [13] © 2008 Elsevier B.V.)



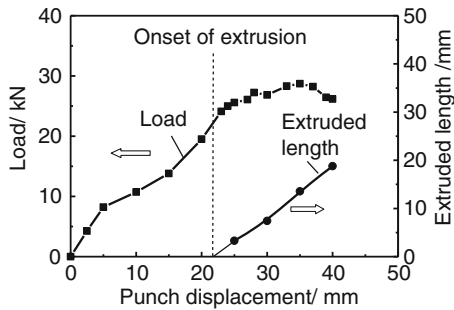
**Fig. 9.15** Schematic illustration of deformation of lotus metals through ECAE process with a channel angle of 90°. It demonstrates the case of porosity of 50 % before the extrusion (Reprinted with permission from [13] © 2008 Elsevier B.V.)

Figure 9.17 shows the diagrams of the punch load–displacement and extruded length. In the beginning of the loading, although the load increases with increasing punch displacement, the extruded length does not increase. In this stage only densification takes place in the entry channel by uniaxial compression. Then at about 20 mm of the punch displacement, the extrusion began and the increment of the extruded length is close to that of the punch displacement. As the initial length of the sample rod is 50 mm, the volume reduction is 40 % when the punch displacement is 20 mm. The value of the volume reduction estimated from the punch displacement agrees well with that estimated from the porosity change. After this stage densification in the entry channel does not take place, but the extrusion is done by shear deformation.

The mechanism of the onset of the extrusion is shown in Fig. 9.18, assuming no friction between the rod and the die. Although the sample is loaded by the punch, the normal force  $F_3$  of the shear flow stress reacts against the punch load  $F_1$ . At the beginning of the pressing, the porosity is as high as 50 % that the compressive flow stress  $\sigma$  of the entry channel by uniaxial compression is smaller than the stress caused by the punch load  $F_1$ , and successively the sample is compressed and densified. During this process, the compressive flow stress  $\sigma$  increases with a



**Fig. 9.16** Cross sections of lotus copper specimens after extrusion approximately 30 mm in a second pass through an ECAE die with a channel angle of 90°. (a) Route A where the direction of the sample of the second pass is the same as that of the first pass. (b) Route C where the direction of the sample of the second pass is 180° turned axially from the first pass (Reprinted with permission from [13] © 2008 Elsevier B.V.)



**Fig. 9.17** Change of the punch load and the extrusion length during the first pass through an ECAE die with a channel angle of 90°. The onset of the extrusion was the place where the increase of the extruded length began (Reprinted with permission from [13] © 2008 Elsevier B.V.)



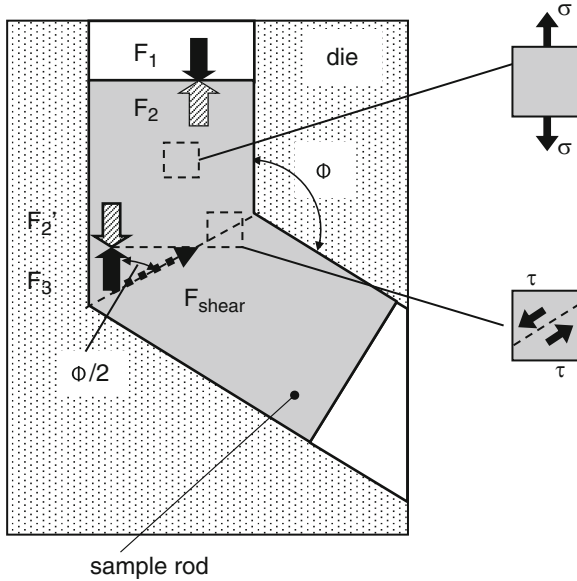


**Fig. 9.18** Mechanical balance model for ECAE process (Reprinted with permission from [13] © 2008 Elsevier B.V.)

decrease of the porosity. It is considered that the force  $F_2$  caused by the compressive flow stress  $\sigma$  is balanced with the force  $F_3$  caused by the shear flow stress  $\tau$  at 20 mm of the punch displacement.

At the beginning of pressing of lotus copper, the load increases slower than that of nonporous metals. At the punch displacement of about 30 mm, the punch load achieved a plateau value. From these results, the criteria for the onset of the extrusion are expressed by the balance of the forces:

$$F_1 = F_2 > F_3.$$

Thus,

$$F_1 = A\sigma > A\tau \cot(\Phi/2), \tag{9.2}$$

where A is the area of the cross section perpendicular to the axis of the entrance channel. Thus, the criteria can be expressed as

$$\frac{\sigma}{\tau} > \cot\left(\frac{\Phi}{2}\right). \tag{9.3}$$

Or  $\Phi = 90^\circ$ , the criteria is expressed as  $\sigma/\tau > 1$ . Although the shear stress  $\tau$  of lotus copper has not been measured exactly, the expression indicates the tendency that the criteria can be satisfied easily when the channel angle  $\Phi$  is large.

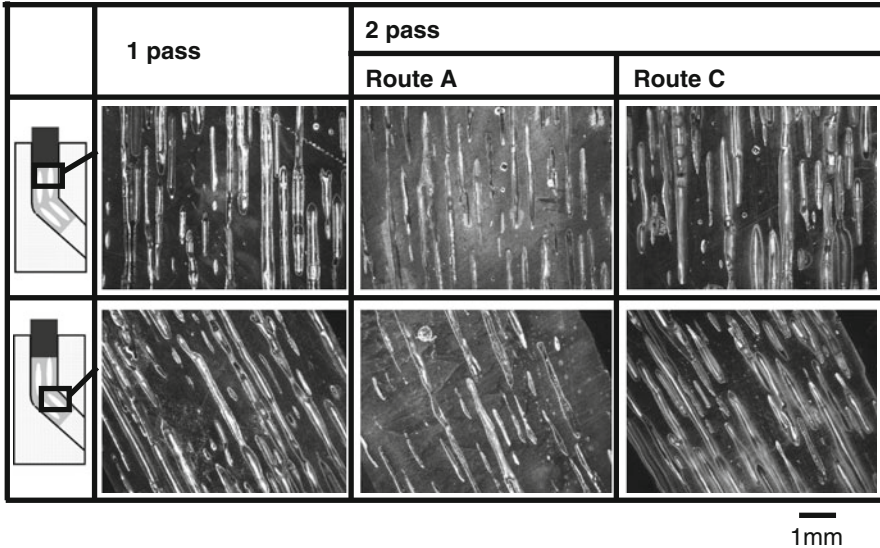
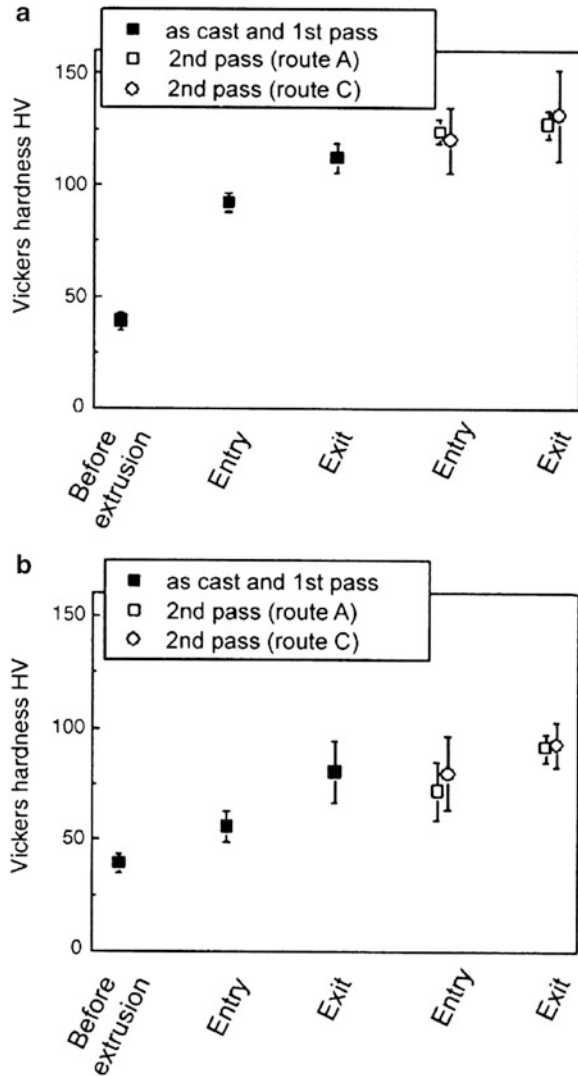


**Fig. 9.19** Cross sections of lotus copper specimens after extrusion in the first and the second pass through an ECAE die with a channel angle of  $150^\circ$  (Reprinted with permission from [13] © 2008 Elsevier B.V.)

If the channel angle of  $150^\circ$  is chosen, an extrusion without densification can be expected. Figure 9.19 shows the cross sections parallel to the sample axis of the extruded sample obtained via 1 pass, route A (2 passes) and route C (2 passes). These photos show that the pore morphology is not changed after 1 pass, and even after 2 passes. Thus, it is concluded that it is possible to extrude without densification under certain suitable conditions.

Figure 9.20a shows the change of the hardness in the case of the channel angle of  $90^\circ$ . During the first pass, the hardness increases in the entry channel because of the densification caused by uniaxial compression. Then, the shear deformation at the corner increases the value of HV. Furthermore, the value of HV increases through both the entry and exit channel of the second pass. There is not so significant difference between route A and C of the second pass. Figure 9.20b shows the HV in the case of the channel angle of  $150^\circ$ . In the entry channel of the first pass, the value of HV is not so different from that before the extrusion. Then in the end channel, HV increases. During the second pass, HV also does not increase in the entry channel and then increases in the exit channel. Compared with the sample extruded through the die with the channel angle of  $90^\circ$ , the increment of the HV is not so large. It is apparent that ECAE process can give work hardening to the sample in the case of channel angle of  $150^\circ$  maintaining the pores. The HV increases with increase of the pass number. Therefore, it is also expected that harder metal with pores after multi-pass ECAE can be obtained through the die with the channel angle of  $150^\circ$ .

**Fig. 9.20** Change of Vickers hardness during the first pass through an ECAE. (a) Channel angle of  $90^\circ$  and (b) channel angle of  $150^\circ$  (Reprinted with permission from [13] © 2008 Elsevier B.V.)



## References

1. Pogibenko AG, Konkevich VY, Arkuzova LA, Ryazantsev VI (2001) *Weld Int* 156:312–316
2. Bollinghaus T, Bleck W (2001) *Cellular metals and metal foaming technology*. MIT, Bremen, pp 495–500
3. Haferkamp H, Ostendorf A, Goede M, Bunte J (2001) *Cellular metals and metal foaming technology*. MIT, Bremen, pp 479–484
4. Murakami T, Nakata K, Ikeda T, Nakajima H, Ushio M (2003) *Mater Sci Eng A* 357:134–140
5. Yamaoka H, Yuki M, Tsuchiya K (2000) *Q J Jpn Weld Soc* 18:422–430
6. Seto N, Katayama S, Matsunawa A (2000) *Q J Jpn Weld Soc* 18:243–255

7. Brandes EA (ed) (1983) Metal reference book, 6th edn. Butterworths, London
8. Watanabe H, Susa M, Nagata K (1997) Metall Mater Trans A 28:2507–2513
9. Murakami T, Tsumura T, Ikeda T, Nakajima H, Nakata K (2007) Mater Sci Eng A 456:278–285
10. Ikeda T, Nakajima H (2002) J Jpn Foundry Eng Soc 74:812–816
11. Ikeda T, Hoshiyama H, Nakajima H (2004) J Jpn Light Metals 54:388–393
12. Asada H, Yoshinaga H (1959) J Jpn Inst Metals 23:67–71
13. Suzuki S, Utsunomiya H, Nakajima H (2008) Mater Sci Eng A 490:465–470
14. Segal VM, Rezinikov VI, Drobyshevkiy AE, Kopylov VI (1981) Russ Metall 1:99–105
15. Valiev RZ, Langdon TG (2006) Prog Mater Sci 51:881–981
16. Hyun SK, Nakajima H (2003) Mater Sci Eng A 340:258–264